

Numerical Simulations of the Sandia Flame D Using the Eddy Dissipation Concept

Dmitry A. Lysenko · Ivar S. Ertesvåg · Kjell Erik Rian

Received: 31 January 2014 / Accepted: 7 July 2014 / Published online: 20 July 2014
© Springer Science+Business Media Dordrecht 2014

Abstract A turbulent piloted methane/air diffusion flame (Sandia Flame D) is calculated using both compressible Reynolds-averaged and large-eddy simulations (RAS and LES, respectively). The Eddy Dissipation Concept (EDC) is used for the turbulence-chemistry interaction, which assumes that molecular mixing and the subsequent combustion occur in the fine structures (smaller dissipative eddies, which are close to the Kolmogorov length scales). Assuming the full turbulence energy cascade, the characteristic length and velocity scales of the fine structures are evaluated using a standard k - ϵ turbulence model for RAS and a one-equation eddy-viscosity sub-grid scale model for LES. Finite-rate chemical kinetics are taken into account by treating the fine structures as constant pressure and adiabatic homogeneous reactors (calculated as a system of ordinary-differential equations (ODEs)) described by a Perfectly Stirred Reactor (PSR) concept. A robust implicit Runge-Kutta method (RADAU5) is used for integrating stiff ODEs to evaluate reaction rates. The radiation heat transfer is treated by the P1-approximation. The assumed β -PDF approach is applied to assess the influence of modeling of the turbulence-chemistry interaction. Numerical results are compared with available experimental data. In general, there is good agreement between present simulations and measurements both for RAS and LES, which gives a good indication on the adequacy and accuracy of the method and its further application for turbulent combustion simulations.

Keywords Reynolds-averaged simulations · Large-eddy simulation · Eddy dissipation concept · RADAU5 · Sandia flame D · Perfectly stirred reactor · OpenFOAM

D. A. Lysenko (✉) · I. S. Ertesvåg
Department of Energy and Process Engineering, Norwegian University of Science and Technology,
Kolbjørn Hejes vei 1B, 7491 Trondheim, Norway
e-mail: dmitry.lysenko@fmcti.com

K. E. Rian
Computational Industry Technologies AS, 7462 Trondheim, Norway

1 Introduction

The long-term goal of the present work is to develop a large-eddy simulation model for high Reynolds number flows of practical interest with further adaptation for turbulent combustion modeling. The core numerical method is based on the OpenFOAM toolbox [55] which was originally developed as a high-end C++ classes library (Field Operation and Manipulation) for a broad range of fluid dynamics applications, but quickly became very popular in industrial engineering as well as in academic research.

Previously, methodical investigations for several plane turbulent bluff-body flows have been carried out with the goal of validation, verification and understanding of the capabilities of the numerical method using the conventional approach for solution of the steady/unsteady compressible Reynolds-averaged Navier-Stokes equations (RANS/URANS), which sometimes referred to as Reynolds-averaged simulations (RAS). These results were analyzed in detail and agreed fairly well with experimental data [32]. It is worth noticing that this detailed investigation and side-by-side comparison of two different codes (ANSYS FLUENT and OpenFOAM) for selected turbulent separated flow problems [32] indicate first of all on the minor influence of the applied numerical method (code) on predictions. Here, we can expect the same behavior for a Sandia Flame D test-case, which is investigated in the present work.

Recently, Lilleberg et al. [31] carried out several turbulent combustion calculations of detailed flame experiments such as the Sandia Flames D,E [2] and a piloted lean lean-premixed jet burner [8, 9]. Lilleberg and his co-workers [31] used a classical approach for the solution of the steady, compressible Reynolds-averaged Navier-Stokes (RANS) equations, where the turbulence was treated via a standard k - ϵ model [29] and adopted several ways to couple chemical kinetics with the Eddy Dissipation Concept [10, 38], including fast chemistry, local extinction and detailed chemistry approaches. As was expected, the detailed chemistry approach showed the best agreement with the measured data for all cases.

Later, the validation of the method was extended for two benchmark flames: the Sandia Flame CHNa [3] and the Sydney Bluff-Body Flame HM1E [7]. Both flames were calculated using the standard k - ϵ model [29]. The turbulence-chemistry interaction was treated via EDC with the detailed chemistry [16] described by the full GRI-3.0 mechanism [4]. In general, there was good agreement between these simulations and measurements for both flames. It is believed that one of the main reasons for the observed discrepancies between the predictions and experimental data was the round-jet anomaly of the k - ϵ turbulence model. Overall, these preliminary results [35, 36] (together with previously obtained results [30, 31]) give a good indication on the adequacy and accuracy of the implemented solver and its readiness for further combustion application development.

In the present study, the method was updated for the combustion LES. Earlier, the LES technique (with several sub-grid scales models) was validated against the flows over a circular cylinder at Reynolds numbers $Re = 3.9 \times 10^3$ [33] and $Re = 2 \times 10^4$ [34]. One of the possible extension of the EDC as a sub-grid scale combustion model for LES was proposed by Panjwani [43]. Here, a more conventional approach to EDC for LES is followed in the simulations of the Sandia Flame D [2].

Thus, the aim of this work is further validation of the OpenFOAM capabilities for RAS/LES applications to the combustion flows of engineering interest. Another scope of this work is to provide high-quality documentation of the implemented method and its detailed validation.

The paper is divided into four main parts. The first and the second parts of the paper describe the mathematical and numerical modeling, respectively. Then, a general description of the test cases is given. Finally, computational results are presented, results are analyzed and discussed, and conclusions are drawn.

2 Mathematical Modeling

One of the most commonly adopted approach in modeling of turbulent reacting flows in the context of RANS/URANS is the Eddy Dissipation Concept (EDC). Initially developed in the 1970s [37], EDC was formulated as a well-established turbulent combustion closure model in the 1990s - 2000s [10, 16, 38].

2.1 Reynolds-averaged simulations

In the present work we will not provide the details of the EDC in the context of Reynolds averaging simulations, see, for example, the authors' previous work [36] for the comprehensive model description. It worth noticing only that in the present study the EDC was coupled with the detailed chemistry approach. For this purpose, the concept of the Perfect Stirred Reactor [16] was utilized with the chemical kinetic mechanism GRI-3.0 [4]. The turbulence was modeled using the standard k - ϵ model [29]. The radiation was treated by the P1-approximation [6].

2.2 Large-eddy simulations

Here, the extension of EDC in the context of the large-eddy simulation is provided.

2.2.1 Governing equations

In present LES, the relevant flow variables are filtered in the physical space (assuming weighted averaging in a given volume). The filtered variable $\bar{f}(x)$ denotes by overbar is defined as

$$\bar{f}(x) = \int_V G(x - x^*) f(x^*) dx^*, \quad (1)$$

where V is the volume of the LES filter and G is a filter kernel. In the present study a top-hat (or sometimes called 'box') filter [15], where the filter operations in each x_j direction are identical, is employed. The filter width Δ is defined as $\Delta = (\Delta_x \Delta_y \Delta_z)^{1/3}$ assuming the filter kernel as

$$G(x) = G(x_1, x_2, x_3) \begin{cases} 1/\Delta & |x_i| < \Delta_i/2, \quad i = 1, 2, 3 \\ 0 & \text{otherwise} \end{cases} \quad (2)$$

where (x_1, x_2, x_3) are the spatial coordinates of the location x .

A mass-weighted, Favre filtering is introduced as:

$$\bar{\rho} \tilde{f}(x) = \int_V \rho G(x - x^*) f(x^*) dx^*. \quad (3)$$

The filtered Favre-averaged balance equations of mass, momentum, energy and species are:

$$\frac{\partial \bar{\rho}}{\partial t} + \frac{\partial \bar{\rho} \tilde{u}_j}{\partial x_j} = 0, \quad (4)$$

$$\frac{\partial \bar{\rho} \tilde{u}_i}{\partial t} + \frac{\partial \bar{\rho} \tilde{u}_i \tilde{u}_j}{\partial x_j} = -\frac{\partial \bar{p}}{\partial x_i} + \frac{\partial \tilde{\tau}_{ij}}{\partial x_j} - \frac{\partial}{\partial x_j} (\bar{\rho} (\tilde{u}_i \tilde{u}_j - \tilde{u}_i \tilde{u}_j)), \quad (5)$$

$$\frac{\partial \bar{\rho} \tilde{Y}_s}{\partial t} + \frac{\partial \bar{\rho} \tilde{Y}_s \tilde{u}_j}{\partial x_j} = \frac{\partial}{\partial x_j} \left(\bar{\rho} D_s \frac{\partial \tilde{Y}_s}{\partial x_j} \right) - \frac{\partial}{\partial x_j} (\bar{\rho} (\tilde{u}_j \tilde{Y}_s - \tilde{u}_j \tilde{Y}_s)) + \bar{\omega}_s, \quad (6)$$

$$\frac{\partial \bar{\rho} \tilde{h}}{\partial t} + \frac{\partial \bar{\rho} \tilde{h} \tilde{u}_j}{\partial x_j} = \frac{\partial}{\partial x_j} (\bar{\rho} \tilde{\xi}_j^h + \tilde{u}_i \tilde{\tau}_{ij}) - \frac{\partial}{\partial x_j} (\bar{\rho} (\tilde{u}_j \tilde{h} - \tilde{u}_j \tilde{h})) + \frac{\partial \bar{p}}{\partial t} - \frac{\partial}{\partial x_j} (\bar{q}_r) + \bar{S}_{hc}, \quad (7)$$

where \bar{f} and \tilde{f} denote Favre-filtered quantities instead of ensemble means. Here, ρ is the density, \mathbf{u} is the velocity, p is the pressure, $h = \sum_s \tilde{Y}_s \int C_{p,s} d\tilde{T}$ represents the enthalpy, T is the temperature, Y_s is the species mass fraction, D_s is the mass diffusion coefficient for species s in a mixture ($D_s = D = 2.88 \times 10^{-5} \text{ m}^2/\text{s}$), ω_s is the species reaction rate, q_r is the radiative heat loss, S_{hc} represents the source term due to combustion and $\tilde{\xi}_j^h$ is the filtered laminar diffusion flux.

\bar{S}_{hc} is modeled according to

$$\bar{S}_{hc} = - \sum_{s=1}^N \frac{\bar{\omega}_s}{M_s} h_{f,s}^\theta, \quad (8)$$

where $h_{f,s}^\theta$ is the species formation enthalpy, M_s is the species molecular weight.

Here, $C_{p,s}$ is calculated as a function of temperature from a set of coefficients taken from NIST-JANAF thermochemical tables [5].

The subgrid flow physics is concealed in the subgrid stress tensor $\mathbf{B} = \bar{\rho} (\tilde{u}_i \tilde{u}_j - \tilde{u}_i \tilde{u}_j)$ and flux vectors $\mathbf{b}_s = \bar{\rho} (\tilde{u}_j \tilde{Y}_s - \tilde{u}_j \tilde{Y}_s)$ and $\mathbf{b}_h = \bar{\rho} (\tilde{u}_j \tilde{h} - \tilde{u}_j \tilde{h})$. The subgrid pressure fluctuations and dissipation terms are neglected. Moreover, the subgrid-scales incompressibility hypothesis [13] is used for derivation of the energy balance equation, assuming low Mach number limit.

It is assumed that the gas mixture behaves as a linear viscous (Newtonian) fluid, which assumes that $\bar{\rho}$, \bar{p} and \bar{T} are linked by the equation of state $\bar{p} = \bar{\rho} R \bar{T}$, where R the composition dependent gas constant.

The shear-stress tensor τ_{ij} is given by

$$\tilde{\tau}_{ij} = 2\mu \tilde{S}_{ij} - \frac{2}{3}\mu \delta_{ij} \tilde{S}_{kk} = 2\mu \tilde{S}_D, \quad (9)$$

where \tilde{S}_{ij} the components of the viscous stress (rate-of-strain) tensor $\tilde{\mathbf{S}}$ defined as,

$$\tilde{S}_{ij} = \frac{1}{2} \left(\frac{\partial \tilde{u}_i}{\partial x_j} + \frac{\partial \tilde{u}_j}{\partial x_i} \right), \quad (10)$$

and μ the viscosity, and

$$\tilde{S}_D = \frac{1}{2} \left(\frac{\partial \tilde{u}_i}{\partial x_j} + \frac{\partial \tilde{u}_j}{\partial x_i} \right) - \frac{1}{3} \delta_{ij} \frac{\partial \tilde{u}_i}{\partial x_j} \quad (11)$$

the deviatoric part of \mathbf{S} .

Explicit LES closures can typically be classified as functional or structural models [13, 49]. Functional models are designed based on the turbulence energy cascade from large-to small-scales considered for the fully-developed turbulent flows. The energy drain for the energy cascade is modeled using the hypothesis of a subgrid viscosity μ_B [11] resulting in

$$\mathbf{B} = \frac{2}{3} \bar{\rho} \delta_{ij} \tilde{k} - 2\mu_B \tilde{S}_D. \quad (12)$$

To close these models, the one equation eddy viscosity model [56] is utilized for which the subgrid viscosity is given by $\mu_B = c_k \bar{\rho} \sqrt{\tilde{k}} \Delta$, and the subgrid kinetic energy \tilde{k} is estimated by solving a separated modeled transport equation of the form,

$$\frac{\partial \bar{\rho} \tilde{k}}{\partial t} + \frac{\partial \bar{\rho} \tilde{k} \tilde{u}_j}{\partial x_j} = \mathbf{F}_p + \mathbf{F}_d - \mathbf{F}_\epsilon, \quad (13)$$

$$\mathbf{F}_p = -\mathbf{B} \cdot \tilde{\mathbf{S}}, \quad (14)$$

$$\mathbf{F}_d = \frac{\partial}{\partial x_j} \left((\mu_B + \mu) \frac{\partial \tilde{k}}{\partial x_j} \right), \quad (15)$$

$$\mathbf{F}_\epsilon = c_\epsilon \bar{\rho} \tilde{k}^{3/2} / \Delta, \quad (16)$$

where \mathbf{F}_p is production, \mathbf{F}_d diffusion and \mathbf{F}_ϵ dissipation terms, respectively, and c_k , c_ϵ are model coefficients. It is worth noticing that both models coefficients can be calculated dynamically using two levels of filtering and scale similarity. However, it was found that the dynamic procedure leads to the numerical instabilities for the combustion LES with the EDC, and static coefficients $c_k = 0.07$ and $c_\epsilon = 1.048$ [49] were used in the present study.

The subgrid fluxes are modeled according to a simple gradient diffusion approximation

$$\mathbf{b}_s = \frac{\mu_B}{Sc_{t,s}} \left(\frac{\partial \tilde{Y}_s}{\partial x_j} \right), \quad (17)$$

$$\mathbf{b}_h = \frac{\mu_B}{Pr_t} \left(\frac{\partial \tilde{h}}{\partial x_j} \right), \quad (18)$$

where $Sc_{t,s}$ and Pr_t are turbulence Schmidt and Prandtl numbers, which were set to $Sc_{t,s} = Pr_t = 0.7$.

2.2.2 EDC for turbulent combustion

The Eddy Dissipation Concept is based on the energy cascade model and assumes that molecular mixing and chemical reactions occur on the smaller dissipative eddies, which are close to the Kolmogorov length scales and are termed fine structures. The characteristic length L^* and velocity u^* scales of the fine structures are of the same order of magnitude as Kolmogorov scales and can be expressed as

$$L^* = \frac{2}{3} \left(\frac{3C_{D2}^3}{C_{D1}^2} \right)^{1/4} \left(\frac{\nu^3}{\tilde{\epsilon}} \right)^{1/4}, \quad (19)$$

$$u^* = \left(\frac{C_{D2}}{3C_{D1}^2} \right)^{1/4} (\nu \tilde{\epsilon})^{1/4}, \quad (20)$$

where $\nu = \mu / \bar{\rho}$ is the kinematic viscosity, $C_{D1} = 0.134$ and $C_{D2} = 0.5$ [10]. Here, we assume that the full cascade takes place at each numerical cell, and the connection between the fine structure and the larger eddies is achieved through the cascade. Thus, characteristics of the large eddies such as velocity u' can be evaluated using the turbulence model. The turbulence kinetic energy \tilde{k} is found from the the solved transport equation (13). The dissipation of the subgrid kinetic energy $\tilde{\epsilon}_{sgs}$ is expressed as

$$\tilde{\epsilon}_{sgs} = c_\epsilon \bar{\rho} \tilde{k}^{3/2} / \Delta, \quad (21)$$

where the model constant $c_\epsilon = 1.048$.

In the model expressed below, different superscripts refer to states inside fine structures (*), surroundings (◦) and filtered values of the computational cell (~).

In this study, the ratio between the mass in the fine structures and the total mass was taken as

$$\gamma^* = \left(\frac{u^*}{u'} \right)^2 = \left(\frac{3C_{D2}}{4C_{D1}^2} \right)^{1/2} \left(\frac{\nu \tilde{\epsilon}}{\tilde{k}^2} \right)^{1/2}, \quad (22)$$

as suggested by Magnussen [39].

The mass exchange between the fine structures and the surroundings, divided by the mass of the fine structures, is defined as

$$\dot{m}^* = 2 \frac{u^*}{L^*} = \left(\frac{3}{C_{D2}} \right)^{1/2} \left(\frac{\tilde{\epsilon}}{\nu} \right)^{1/2}. \quad (23)$$

The mass exchange between the fine structures and the surroundings, divided by the total mass, is calculated according to

$$\dot{m} = \gamma^* \dot{m}^*. \quad (24)$$

The mass-averaged filtered reaction rate for the s -th specie is given as

$$-\bar{\omega}_s = \frac{\bar{\rho} \dot{m} \chi}{1 - \gamma^* \chi} (\tilde{Y}_s - Y_s^*), \quad s = 1, \dots, N_s \quad (25)$$

and the relationship between the mass-averaged mean state, fine-structure state and surrounding state is expressed as

$$\tilde{\Psi} = \gamma^* \chi \Psi^* + (1 - \gamma^* \chi) \Psi^\circ. \quad (26)$$

Here, χ is the reacting fraction of the fine structures, which can depend on probability of co-existence of the reactants, degree of heating and a limiter to the reaction due to lack of reactants. In the present study, $\chi = 1$, as suggested by Gran and Magnussen [16]. The mass fraction \tilde{Y}_s for species s is calculated from solving the species mass transport equation for each individual species. The fine-structure mass fraction Y_s^* is computed through the detailed chemistry approach.

The expression of Eq. 22 [39] represents a change compared to former versions of EDC [16, 38], which had $\gamma^* = (u^*/u')^3$. In isotropic turbulence, the ratio of Eq. 22 will be proportional to Re_λ^{-1} , where Re_λ is the turbulence Reynolds number based on the Taylor microscale. The previously used expression will be proportional to $\text{Re}_\lambda^{-3/2}$. The change has an effect in the RHS denominator of Eq. 25 and in Eq. 26. There is, however, no formal effect in the numerator of Eq. 25. Besides this, there is a change in interpretation. The previous model corresponds to a sheet-like turbulence fine structure (Corrsins model), whereas Eq. 22 corresponds to a tube-like structure (Tennekes model), see [10].

2.2.3 The finite-rate chemistry approach

Finite-rate chemical kinetics are taken into account by treating the fine structures as constant pressure and adiabatic homogeneous reactors. Thus, the fine structures mass fractions values Y_s^* can be calculated by solving a system of ODEs describing a Perfectly Stirred Reactor (PSR) [16],

$$\frac{dY_s^*}{dt} = \frac{\omega_s^*}{\rho^*} + \frac{1}{\tau^*} (Y_s^\circ - Y_s^*), \quad s = 1, \dots, N_s. \quad (27)$$

The reaction rate ω_s^* is evaluated from a chemical kinetics mechanism. Y_s° is the mass fraction of the inflow stream to the reactor (cf. Eq. 26). In the present study, it is assumed

adiabatic and isobaric PSRs. Further, it is assumed that the PSRs are at steady state [16], meaning that the steady-state solution of Eq. 27 is achieved by integrating it in time to steady state.

It is worth noticing that the residence or mixing time scale τ^* is evaluated using the molecular viscosity and the dissipation rate

$$\tau^* = \frac{1}{\dot{m}^*}. \quad (28)$$

In the present study the chemistry was treated by the single step mechanism:



with the following rate parameters: $A = 9.49 \times 10^{11}$ [m, kg, mol, s], $\beta = 0$, $T_a = 23650$ K, $n_{\text{CH}_4} = 0.7$ and $n_{\text{O}_2} = 0.8$. Applying of more detailed kinetic schemes such as the GRI3.0 mechanism is still computationally expensive and was out of scope of the present work.

2.3 The mixture fraction probability density function model

In the present study the mixture fraction, f is defined as [53]

$$f = \frac{Z_i - Z_{i,ox}}{Z_{i,fuel} - Z_{i,ox}}, \quad (30)$$

where Z_i is the elemental mass fraction for element i . The subscripts ox and fuel denote the value at the oxidizer and fuel stream inlets, respectively. Using the standard assumptions of the equal diffusion coefficients for all species, and assuming that the considered flow is turbulent (where turbulent convection overwhelms molecular diffusion), f is the elemental mass fraction. Equation 30 is identical for all elements when the diffusion coefficients are equal for all species. In this case the mixture fraction is the elemental mass fraction that originated from the fuel stream [1].

The Favre-mean transport equation for \tilde{f} and its variance $\widetilde{f''^2}$ [1, 27] are

$$\frac{\partial}{\partial t} (\bar{\rho} \tilde{f}) + \frac{\partial}{\partial x_j} (\bar{\rho} \tilde{u}_j \tilde{f}) = \frac{\partial}{\partial x_j} \left(\frac{\mu_t}{\text{Sc}_t} \frac{\partial \tilde{f}}{\partial x_j} \right), \quad (31)$$

$$\frac{\partial}{\partial t} (\bar{\rho} \widetilde{f''^2}) + \frac{\partial}{\partial x_j} (\bar{\rho} \tilde{u}_j \widetilde{f''^2}) = \frac{\partial}{\partial x_j} \left(\frac{\mu_t}{\text{Sc}_t} \frac{\partial \widetilde{f''^2}}{\partial x_j} \right) + C_g \mu_t \left(\frac{\partial \tilde{f}}{\partial x_j} \right)^2 - C_d \bar{\rho} \frac{\tilde{k}}{\tilde{\epsilon}} \widetilde{f''^2}, \quad (32)$$

where $f'' = f - \tilde{f}$, $\text{Sc}_t = 0.85$, $C_g = 2.86$ and $C_d = 2$.

For the Reynolds-averaged calculations, \tilde{k} and $\tilde{\epsilon}$ are retrieved from the transport equations of the standard k - ϵ model [29].

For the large-eddy simulation, $\widetilde{f''^2}$ is modeled according to

$$\widetilde{f''^2} = C_k L_s^2 \left| \frac{\partial \tilde{f}}{\partial x_j} \right|^2, \quad (33)$$

where L_s is the mixing length for sub-grid scales and C_v is constant. The mixing length scale is computed as

$$L_s = \frac{\tilde{k}^{3/2}}{\tilde{\epsilon}}, \quad (34)$$

where \tilde{k} is retrieved from the transport (13) and $\tilde{\epsilon}$ is calculated according to Eq. 21. The constants C_k and Sc_t are computed by applying the dynamic procedure proposed by Germano

[14]. It worth noticing that both constants c_k and c_ϵ from Eq. 13 for the assumed β -PDF approach are computed dynamically as well.

In the present study a chemical equilibrium assumption is used, where reactions rates are sufficiently fast for the mixture to be in a state of chemical equilibrium. With this assumption the equilibrium state of density, temperature and composition can be obtained by minimizing the free energy [53].

In AF the values of density, temperature and species mass fractions are determined from look-up tables, depending on mean and variance of the mixture fraction and the enthalpy

$$\tilde{\phi}_i = \tilde{\phi}_i(\tilde{f}, \widetilde{f'^2}, \tilde{h}). \quad (35)$$

These tabulated values are obtained by a prescribed PDF, $p(f)$, modeled by a β function and a Dirac delta PDF, $\delta(h - \tilde{h})$. The latter means that enthalpy fluctuations are assumed independent of the amount of heat transferred. The procedure requires solution of the model transport equation for the enthalpy [1, 21]

$$\frac{\partial}{\partial t}(\bar{\rho}\tilde{h}) + \frac{\partial}{\partial x_j}(\bar{\rho}\tilde{u}_j\tilde{h}) = \frac{\partial}{\partial x_j}\left(\frac{\mu_t}{Pr_t}\frac{\partial \tilde{h}}{\partial x_j}\right) - \frac{\partial}{\partial x_j}(\bar{q}_r), \quad (36)$$

where the AF default value of the turbulence Prandtl number was used, $Pr_t = 0.7$.

2.4 Modeling radiation

The radiation is modeled by the P1-approximation, which is the simplest form of the more generalized P-N method (or spherical harmonics) [6] assuming that a flame is optically thin. The radiative heat loss \bar{q}_r is calculated as

$$-\frac{\partial}{\partial x_j}\bar{q}_r = \alpha_c G - 4e_c\sigma T^4, \quad (37)$$

where α_c is the absorption coefficient (m^{-1}), e_c is the emission coefficient (m^{-1}) and σ is the Stefan-Boltzmann constant. The incident radiation G is modeled according to

$$\frac{\partial}{\partial x_j}\left(\Gamma\frac{\partial}{\partial x_j}G\right) - \alpha_c G + 4e_c\sigma T^4 = 0, \quad (38)$$

$$\Gamma = \frac{1}{3(\alpha_c + \sigma_s)}, \quad (39)$$

where σ_s is the scattering coefficient ($\sigma_s = 1 \text{ m}^{-1}$), respectively. The absorption coefficient and the emission coefficient are calculated using a weighted-sum-of-gray-gases model (WSGGM) [22] as a function of local concentrations of CO_2 and H_2O , path-length and pressure. The emissivity weighting factors for CO_2 and H_2O are taken from Smith et al. [51].

3 Brief Description of the Numerical Methodology

The main emphasis of this work was put on the problem of validation of the Eddy Dissipation Concept implemented in the OpenFOAM (hereafter OF) toolbox [55]. However, to investigate the influence of the turbulence-combustion interaction modeling, the assumed β -PDF approach was tested as well using the ANSYS FLUENT (hereafter AF) technology [1]. It worth noticing, that the same grids were used for both solvers. The standard k - ϵ model [29] (SKE hereafter) with wall functions and the one-equation eddy-viscosity SGS model

[56] (TKE hereafter) were used for the closure problem for URANS and LES, respectively. The radiative heat transfer was treated using the P-1 approximation.

3.1 OpenFOAM

The OpenFOAM code [55] was used for the EDC-based simulations. The solver was developed based on the finite-volume (FVM) method [15] and the PISO (pressure implicit with splitting of operators) algorithm [52] for the pressure-velocity coupling, implemented according to Rhie and Chow type interpolation for the cell-centered data storage structure [24]. The conjugate gradient method [19] with incomplete Cholesky decompositions of Meijerink and van der Vorst [42] was used for solving the system of linear algebraic equations with a local accuracy of 10^{-9} for all dependent variables at each time step for RAS, while a smooth solver (with a Gauss-Seidel smoother) was used for LES.

The numerical method had second-order accuracy in space and time. The linear-upwind interpolation scheme (the second-order upwind scheme [54]) and linear (second-order central differences, CDS-2) interpolation were applied for convective terms approximation and other spatial derivatives, respectively, for RAS calculations.

For the large-eddy simulations, the Gamma scheme by Jasak et al. [25] was applied for the momentum equation convective-term approximations, which is a bounded form of CDS-2. The blending was controlled by a parameter, γ , which was set to $\gamma = 0.15$. As is common practice for reacting LES [28, 44], a total variation diminishing (TVD) scheme [18] was used for the scalars to avoid unphysical overshoots and second law violations.

A second-order implicit Euler method (BDF-2 [15]) was used for time integration together with the dynamic adjustable time stepping technique to guarantee a local Courant number less than 0.4 both for RAS and LES.

The calculation of the species reaction rate $\bar{\omega}_s$ requires the integration of Eq. 27 for each computational cell in the domain. For this purpose, the robust RADAU5 algorithm [17] was used. The RADAU5 algorithm is designed for the solving stiff ODE systems and applies a 5th order accurate implicit Runge-Kutta method based on the Radau quadrature formula. The relative tolerance, absolute tolerance and maximum number of iterations to meet the target accuracy were set to 5×10^{-5} , 10^{-5} and 10^7 , respectively.

3.2 ANSYS FLUENT

Using the factorized FVM [15], the RANS equations were solved with a second-order accuracy in space and time. The velocity and pressure fields were matched with a centered computational template based on the SIMPLEC [52] algorithm within the spirit of Rhie and Chou [48]. The convective terms were represented according to the Leonard quadratic upwind scheme (QUICK) [54] for RAS, while the bounded CDS-2 and second-order upwind schemes were used for LES for the momentum and other scalars, respectively. The linear system of equations was solved with GaussSeidel smoother, which was accelerated by an algebraic multi-grid (AMG) technique, based on the additive-correction strategy [23]. LES was carried out using implicit dual-stepping technique with the fixed time step of 10^{-5} s.

3.3 High performance computing

OpenFOAM is the massive parallel open source C++ classes library based on message-passing interface (MPI). The most of the present calculations were carried out using Vilje

HPC facility (www.notur.no). RAS calculations were carried out using 32 cores in parallel, while LES simulations were performed using 80 cores. In general, it was required approximately 2 weeks for RAS and 3 – 4 weeks for LES to achieve statistically converged solutions.

4 Test Case Description

4.1 Experimental setup

The Flame D from the Sandia/TNF workshop is a piloted methane-air diffusion flame [2]. The central main jet consisted of a methane-air mixture (with 25 % by volume of CH_4) corresponding to an equivalence ratio of 3.174. This is above the upper flammability limit of methane so combustion is still controlled by mixing. It was surrounded by a pilot flame and a slow coflow of air outside. The bulk velocities of the main jet, pilot and coflow were $U_\infty = 49.6$ m/s, $U_p = 11.4$ m/s and $U_c = 0.9$ m/s, respectively. The main jet nozzle had an inner diameter (d) of 7.2×10^{-3} m, which resulted in a jet Reynolds number, $\text{Re}_j =$

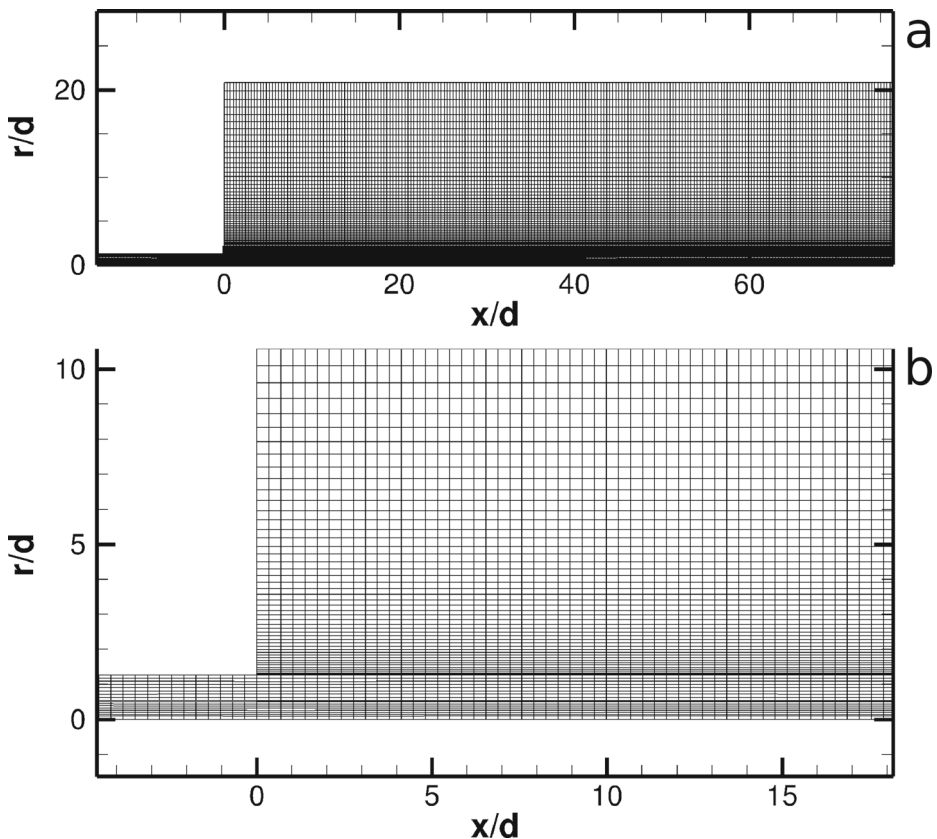


Fig. 1 General view of the computational domain **a** and details of the grid near the inlet **b** for the Sandia Flame D. x and r are the domain coordinates in axial and radial direction

$U_{\infty}d/\nu = 2.24 \times 10^4$, where ν is the main jet kinematic viscosity, $\nu = 1.58 \times 10^{-5} \text{ m}^2/\text{s}$. Flame D exhibited local extinction to a limited degree [2]. The pilot flame was burning a mixture of C_2H_2 , H_2 , air, CO_2 , and N_2 with an enthalpy and equilibrium composition that is equivalent to a mixture of methane and air at an equivalence ratio of $\phi = 0.77$. The pilot annulus inner and outer diameters were $7.7 \times 10^{-3} \text{ m}$ and $18.2 \times 10^{-3} \text{ m}$, respectively. The experimental data was documented in detail by Barlow and Frank [2].

4.2 RAS grids and boundary conditions

Some details of the RAS computational domain are shown in Fig. 1. The axial and radial dimensions of the computational domain after the burner exit were set to $76.5 \times d$ and $20.83 \times d$, respectively. The EDC-based simulations were carried out for two grids. The coarse grid had 110 and 40 cells along the axial and radial directions, respectively. The jet pipe was resolved with 4 cells, and the pilot was resolved with 5 cells, in the radial direction. The length of the pre-inlet fuel and pilot pipes were approximately $15 \times d$. The second

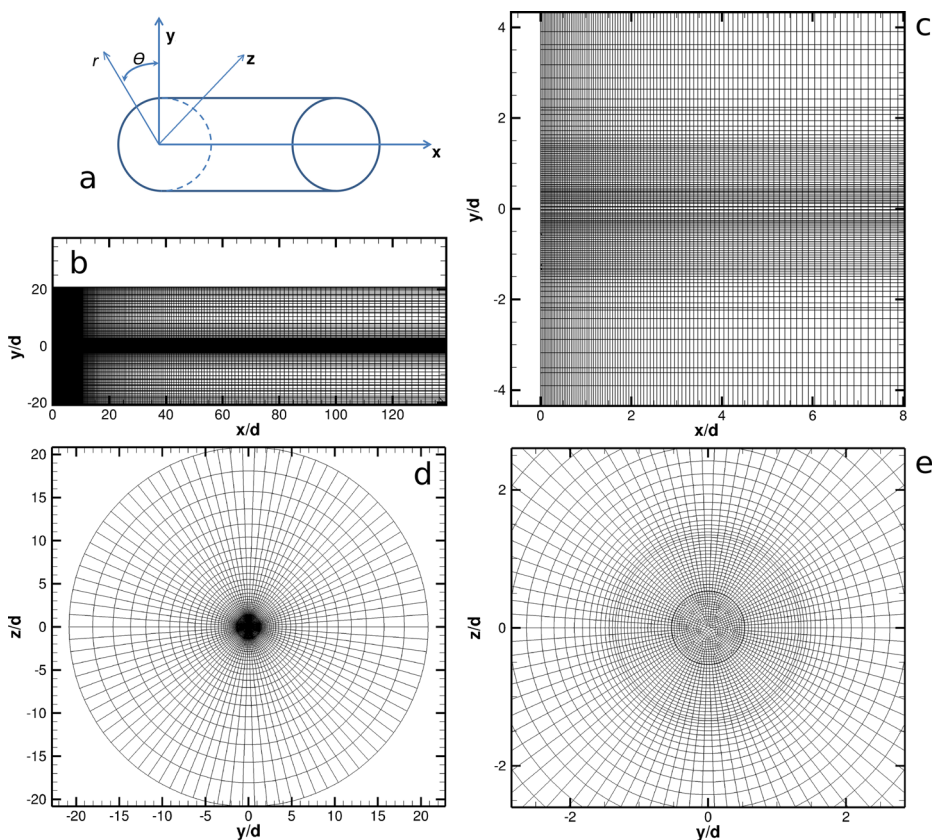


Fig. 2 Details of the LES-A1 grid: general scheme **a**, description of the grid in $x-y$ **b** and $y-z$ **d** planes and zoom of the grid in $x-y$ **c** and $y-z$ **e** planes for the Sandia Flame D. x , y and z are the domain coordinates in stream-wise, transverse and span-wise directions, θ and r are the circumferential and radial coordinates, respectively

mesh was designed just by a subsequent grid refinement by factor 2 in both radial and axial direction. Details of the fine grid are presented in Fig. 1.

In general, the differences between EDC-based results obtained on these grids were insignificant for the mean velocities, temperature and main species such as O_2 , N_2 , CO_2 , H_2O and H_2 . However, for the intermediate species such as CO , OH and NO , high-resolution grid provides more accurate results. Therefore, all present EDC-based and β -PDF-based results discussed below were obtained using the high-resolution grid (termed hereafter RAS-A2). Further grid refinement was not carried out due to resource limitations.

The problem was solved assuming symmetry about the centerline. The computational domain was designed as a sector of 5° with imposed periodic boundary conditions and included pre-inlet pipes for the fuel-jet and pilot in order to obtain fully-developed turbulent velocity profiles. Uniform velocity profiles were specified for the jet, pilot and co-flow. All radial and circumferential velocity components were set to be zero. The inflow temperatures were set based on the experimental settings. The exit pressure was specified to 10^5 Pa at the outlet, and zero-gradient pressure was imposed at the inlet boundaries. A non-slipping condition for velocity was applied for all walls. Wall-functions were set for k and ϵ . The temperature at the walls was calculated according to the zero gradient boundary condition. The fuel jet, pilot and co-flow compositions were specified in terms of the species mass fractions calculated from the experimental data. Marshaks boundary conditions [40], based on solutions of Legendre polynomials of odd order, were adopted for radiative heat flux calculations.

4.3 LES grids and boundary conditions

Two grids (termed hereafter LES-A1 and LES-A2) were used in this study for LES. The axial and radial dimensions of the computational domain for the A1 grid (Fig. 2) were set

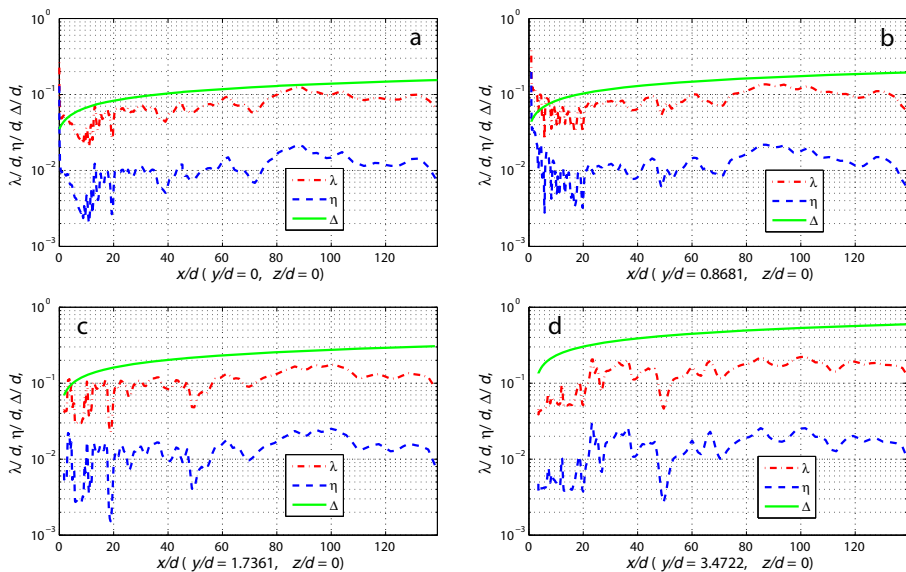


Fig. 3 Comparison of axial distributions of subgrid filter, Taylor and Kolmogorov scales at four different radial states obtained for the LES-A1 grid for the Sandia Flame D

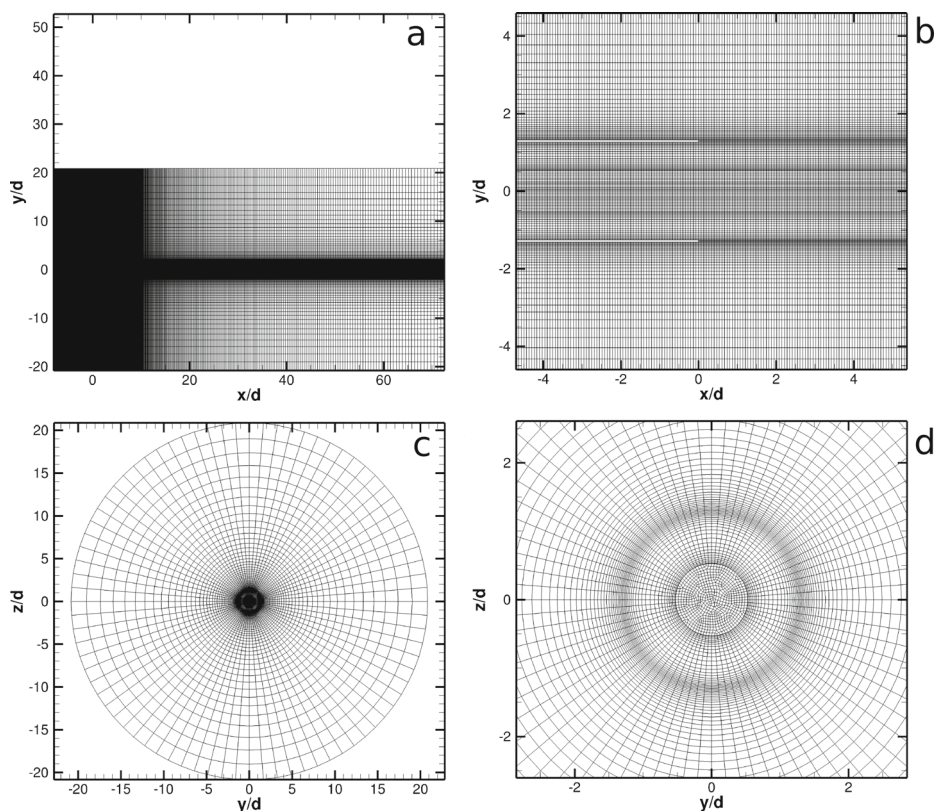


Fig. 4 Details of the LES-A2 grid: description of the grid in $x - y$ **a** and $y - z$ **c** planes and zoom of the grid in $x - y$ **b** and $y - z$ **d** planes for the Sandia Flame D

to $139 \times d$ and $20.83 \times d$, respectively. The resolution of the A1 grid was $240 \times 60 \times 90$ in the axial, radial and circumferential directions with the grid clustering applied to the jet and pilot with the purpose to resolve the strong gradients that arise near the inlet. Both, the jet pipe and the pilot were resolved with 18 cells in the radial direction. LES-A1 mesh was designed without any pre-inlets.

Table 1 Run matrix

Run	C	TM	TCM	CH	R	M
ke-EDC-GLB	OF	SKE	EDC	Single Step	P1	RAS-A2
ke-EDC-GRI3	OF	SKE	EDC	GRI3.0	P1	RAS-A2
ke- β -PDF	AF	SKE	β -PDF	–	P1	RAS-A2
A1-LES-EDC-GLB	OF	TKE	EDC	Single Step	P1	LES-A1
A2-LES-EDC-GLB	OF	TKE	EDC	Single Step	P1	LES-A2
A1-LES- β -PDF	AF	TKE	β -PDF	–	P1	LES-A1

As it is customarily done in practice, some estimation of resolution of the LES-A1 grid based on the Taylor ($\lambda^2 = 10\nu \langle K \rangle / \langle \tilde{\epsilon}_{sgs} \rangle$) and Kolmogorov scales ($\eta = (v^3 / \langle \tilde{\epsilon}_{sgs} \rangle)^{1/4}$) was provided. Here, the mean resolved turbulence kinetic energy was calculated according to $\langle K \rangle = 1/2 \langle \mathbf{u}'\mathbf{u}' \rangle$. The mean dissipation rate was assumed to be equal to the mean subgrid dissipation rate $\langle \tilde{\epsilon}_{sgs} \rangle$ (21). The mean kinematic viscosity was not assembled while data sampling, thus its instantaneous values were used. Figure 3 displays axial distributions of the subgrid filter, Taylor and Kolmogorov scales at several radial states. Quite obviously, the Kolmogorov scales were located more than a decade lower than Taylor scales. It is clearly also, the subgrid filter scales were the same order as Taylor micro-scales in the jet nozzle and pilot annulus regions where the grid clustering was applied. Further, the resolution of the grid progressively decreasing starting approximately from the pilot outer diameter towards the outlet boundaries.

The A2 grid (Fig. 4) was designed with the purpose to investigate the effect of the inlet boundary conditions. The axial and radial dimensions of the computational domain for the A2 grid were set to $72.5 \times d$ and $20.83 \times d$ with the subsequent resolution of $460 \times 80 \times 80$ in the axial, radial and circumferential directions. The pre-inlet section of the grid for the jet, pilot and co-flow (Fig. 2c) had the axial length of $8.05 \times d$ with the uniform axial spacing with 120 cells. The jet pipe, the pilot and co-flow were resolved with 20, 20 and 40 cells in the radial direction, respectively. The grid clustering was applied in radial direction to resolve strong shear layers between jet, pilot and co-flow.

5 Results and Discussion

5.1 Present predictions

All simulated cases are listed in Table 1 (where the following abbreviations are used: C – code OF or AF, TM – turbulence model (SKE or TKE), TCM – turbulence-chemistry interaction model (EDC or β -PDF), CH – chemistry mechanism, R – radiation sub-model, M – mesh). For the single step mechanism, see Eq. 29.

Time-averaged results from the simulations are discussed and compared with the experimental data by Schneider et al. [50], who performed LDV velocity measurements, and Barlow and Frank [2], who measured the temperature and the concentrations of chemical species. The sampling of data is of great importance for any transient simulations. In the present calculations one-two flow-through times were used for RAS results. It can be shown that for this particular case it is enough to obtain asymptotically converged mean results. 10-20 flow-through times were used for the LES runs based on the results discussed

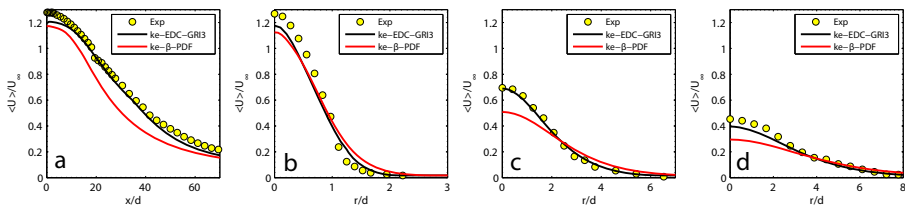


Fig. 5 Comparison of predicted and measured mean axial velocity along the axis **a** and at $x/d = 7.5$ **b**, $x/d = 30$ **c** and $x/d = 45$ **d** for the Sandia Flame D

in the literature [28] and mostly due to resource limitations. However, it will be interesting in future to investigate the influence of the averaging interval on an accuracy of results. Here, the flow-through time is defined as the ratio between the axial length of the computational domain to the jet bulk velocity. Hereafter, the time-averaging operator is denoted by $\langle \rangle$. The tilde mark denoting Favre-averaging (or filtered Favre-averaging) is omitted for the simplicity.

5.2 RAS results

Figure 5 displays axial and radial distributions of the mean axial velocities. In general, good agreement between predictions and experimental data could be observed. One can see, that the present results under-estimated to some extent the jet velocity along the central axis. The divergence between the β -PDF approach and the measured data was more significant and could be possibly explained by the compressibility effects. Hewson and Kerstein [20] carried out a detailed investigation of such phenomena and suggested that the dilatation of the flow was a possible explanation for these discrepancies. According to Hewson and Kerstein [20] dilatation pushes the fluid downstream leading to higher mixture fractions on the axis and affecting the dissipation rate. Agreement between calculations and measurement along the centerline as well as between radial profiles at $x/d = 7.5$ was very satisfactory. At $x/d = 30$ and $x/d = 45$ the calculated velocities were slightly lower (especially for the assumed β -PDF approach) compared to the experimental data which indicated that the decay of the jet was under-estimated and can be explained by using the standard k - ϵ model with a not-corrected $C_{\epsilon 1}$ constant [41, 46].

A comparison of the predicted flame temperatures is displayed in Fig. 6. Scalar data are presented in Fig. 7. Along the central axis, the peak mean temperature agreed well with the experimental data. The maximum peak temperatures obtained by all runs $\langle T_p \rangle = 1955 - 1960$ K matched well the measured peak temperature $\langle T_p \rangle = 1945$ K. One can

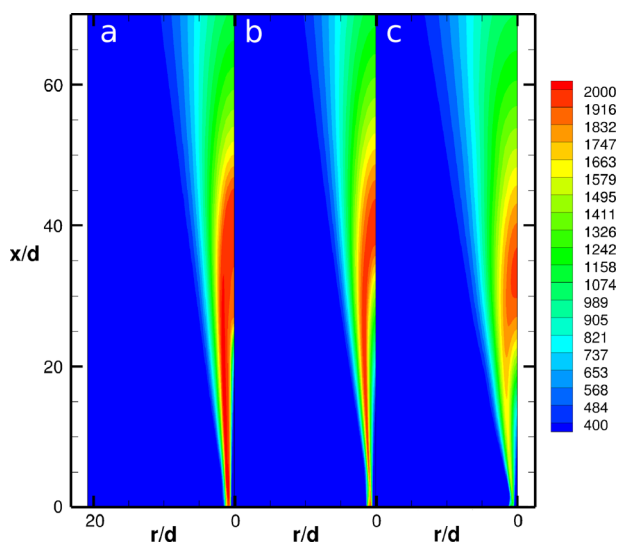


Fig. 6 Iso-contours of mean temperature (K) for the Sandia Flame D: ke-EDC-GLB **a**, ke-EDC-GRI3 **b** and ke- β -PDF **c**

observe a small shift between predicted and measured peak locations approximately of $6 \times d$ for the β -PDF approach which can be explained by the dilatation effect [20]. The worst prediction was obtained by the EDC-based approach where the single-step chemistry was used.

The calculated mean species $\langle Y_{O_2} \rangle$, $\langle Y_{N_2} \rangle$, $\langle Y_{H_2} \rangle$, $\langle Y_{H_2O} \rangle$, $\langle Y_{CO_2} \rangle$, $\langle Y_{CO} \rangle$ and $\langle Y_{CH_4} \rangle$ by the EDC-based approach with the GRI3.0 chemistry had the similar behavior as the mean temperature and reasonably agreed with the experimental data. Strong deviations were observed only for $\langle Y_{OH} \rangle$, $\langle Y_{NO} \rangle$ which showed only the correct trends.

The production of NO is highly dependent on temperature. Thus, one of the possible reasons for such discrepancies may be the incorrect treatment of radiation which can have a significant effect on the predicted NO levels [12]. In the present study an optically thin assumption was used for the treatment of the radiative losses. Frank et al. [12] showed that the optically thin radiation sub-model did not accurately predict the radiant fraction for this flame which reflects the complexity of the NO formation process. Based on spectral characteristics of the radiant emission and transmittance, they found that an optically thin assumption was inappropriate for partially premixed CH_4 /air jet flames. Thus, it will be interesting in future work to calculate this flame with another radiation sub-model.

Prediction of OH in any combustion simulation is particularly challenging due to the strong nonlinearity of the species evolution [47]. The level of agreement displayed by OH was reasonable good, however the calculated maximum mass fraction was over-predicted significantly compared with the respected measured data.

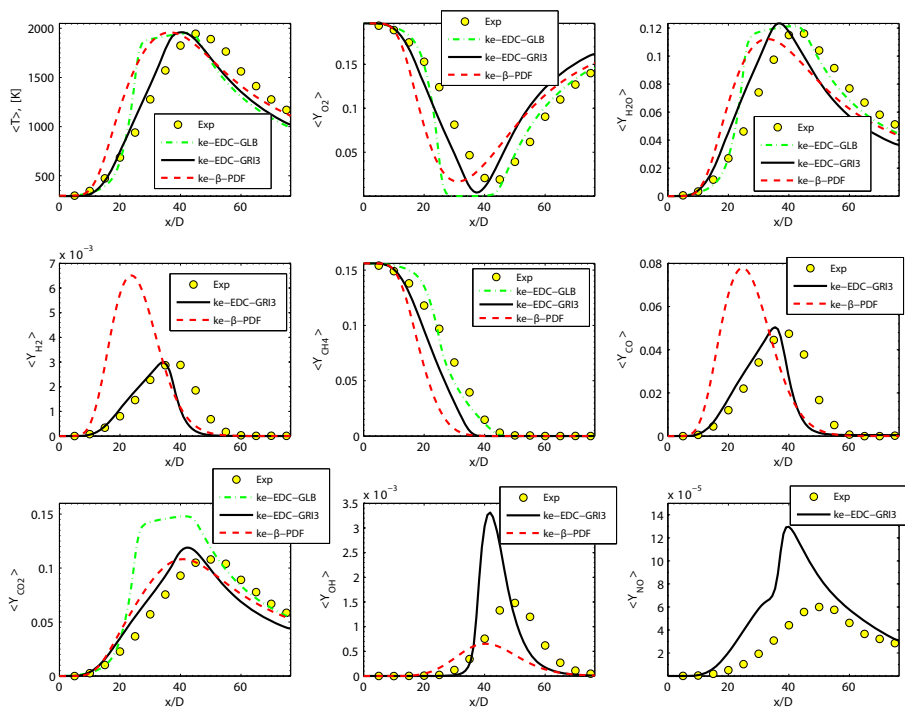


Fig. 7 Influence of the turbulence-chemistry interaction model for the Sandia Flame D: mean temperature and mean composition profiles along the axis

In general, the predictions of the flame was in good agreement with the reported measurements. It should also be noted that the choice of the detailed chemical reaction mechanism affects the prediction of the peak values and peak positions of the scalars, especially minor species, such as CO, OH and NO [31]. In this study, the full GRI-Mech 3.0 mechanism [4] was used. Choosing another chemical kinetic mechanism with the same level of detail would have given slightly different predictions but minor differences for the major species and the temperature [57].

5.3 LES results

Figure 8a,b shows instantaneous temperature fields of the computed flow. Figure 8c gives an overview of the local coherent structures visualized by means of λ_2 (defined according to Jeong and Hussain [26]) at the same instance. It is interesting to note that close to the nozzle, the region around the reaction zone was dominated by the molecular diffusion and hardly showed turbulent motion and might be regarded as being laminar [44]. This phenomena has been found in many experiments and can be explained by the fact that fuels with Lewis numbers different from unity were sources of strong differential diffusion effects, which could survive even far downstream of the transition to turbulence [44, 45]. Further downstream, the formation of large-scale coherent structures took place due to the growth of perturbations. The iso-surface of λ_2 identified the vortex cores that originate from the roll-up of the shear layer between jet flow and pilot and between pilot and co-flow which are convected further downstream by the mean flow.

Figures 9 and 10 compare one-dimensional Fourier energy spectra and one-dimensional wavelet energy spectra (illustrates the time-frequency evolution of the scalogram) extracted from the run A2-LES-EDC-GLB at downstream locations ($x/d = 10$ and $x/d = 20$) on the centerline of the wake. The spectral analysis was done in the same manner as in our

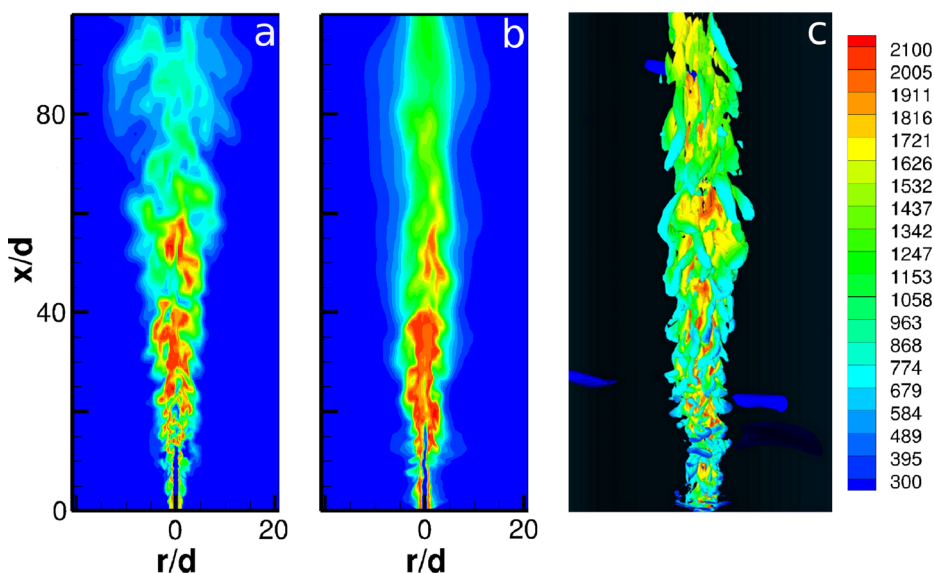


Fig. 8 Instantaneous iso-surfaces of temperature (K) obtained by A1-LES- β -PDF **a**, A1-LES-EDC-GLB **b** and λ_2 visualization (colored by temperature) by A1-LES-EDC-GLB **c** for the Sandia Flame D

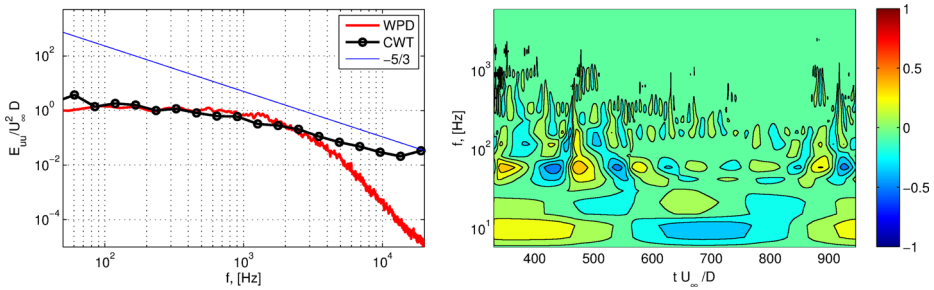


Fig. 9 Fourier power spectra (WPD) and wavelet coefficient energy (CWT) with its associated scalogram of the axial velocity at $x/d = 10$ obtained by A2-LES-EDC-GLB for the Sandia Flame D

previous work [34]. One can see that the flow near the axial location $x/d = 10$ was mostly laminar and became turbulent further downstream ($x/d = 20$). The inertial subrange was reproduced clearly for a large spectral range, assuming that sub-grid modeling was not over-dissipative and the flow was fully turbulent at $x/d = 20$. Moreover, the spectra were also consistent with the presence of small scales that can be observed clearly at the scalogram displayed in Fig. 10.

The mean axial velocity and its root-mean-square (RMS) values along the centerline are displayed in Fig. 11. All runs were in reasonable agreement with the experimental data, although the RMS values obtained by the EDC-based approach seem to be under-predicted in the core region of the jet where combustion takes place. However, such discrepancies could be explained by the the nature of the applied inlet boundary condition, insufficient grid resolution and the effects of the applied TVD schemes leading to the limited resolution of the finest scales.

A strange peak in the mean axial velocity distribution obtained by A2-LES-EDC-GLB was observed in Fig. 11a located somewhere between $20 \times d$ and $30 \times d$. This unphysical behavior, probably, could be explained by the design of the A2 grid. Indeed, the A2 grid had the uniform cell distribution along the axis up to $x/d \sim 10$ whereupon the sudden grid expansion (coarsening) started. It is well known that spurious solution oscillations could be observed quite often while numerical approximation of compressible flow equations on non-uniform grids [34].

The calculated mean temperature and mean mass fractions of O_2 , N_2 , CH_4 , CO_2 and H_2O and their RMS values along the centerline are shown in Figs. 12 and 13. In general

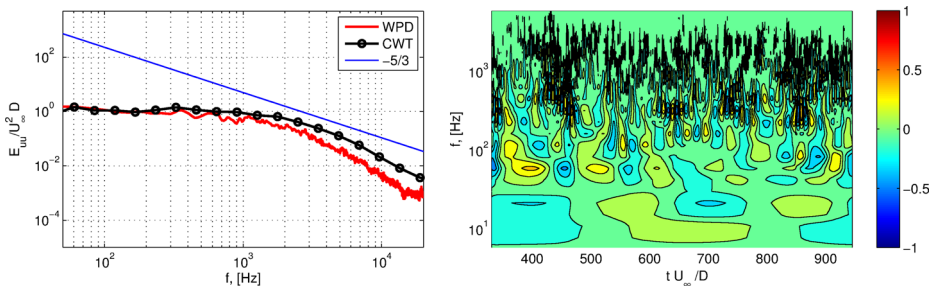


Fig. 10 Fourier power spectra (WPD) and wavelet coefficient energy (CWT) with its associated scalogram of the axial velocity at $x/d = 20$ obtained by A2-LES-EDC-GLB for the Sandia Flame D

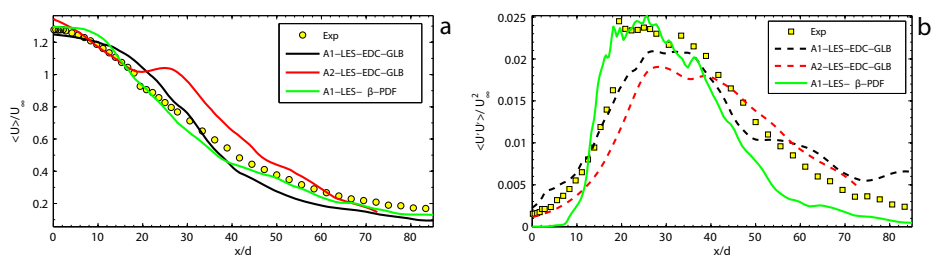


Fig. 11 Mean axial velocity **a** and its fluctuations **b** along the axis for the Sandia Flame D

all profiles agreed reasonably with the experimental data. The mean temperature profiles collapsed well with the experimental data for all runs. However, it seems that transition to the turbulence was slightly delayed by A2-LES-EDC-GLB and A1-LES- β -PDF. The predicted fluctuations of the temperature matched reasonably the experimental data. One can observe some discrepancies between predicted and measured values of the temperature RMS around the first peak (approximately at $x/d = 30$) caused mainly due to sudden heat release and expansion of the gases near the nozzle which leads to the production of momentum and turbulence kinetic energy.

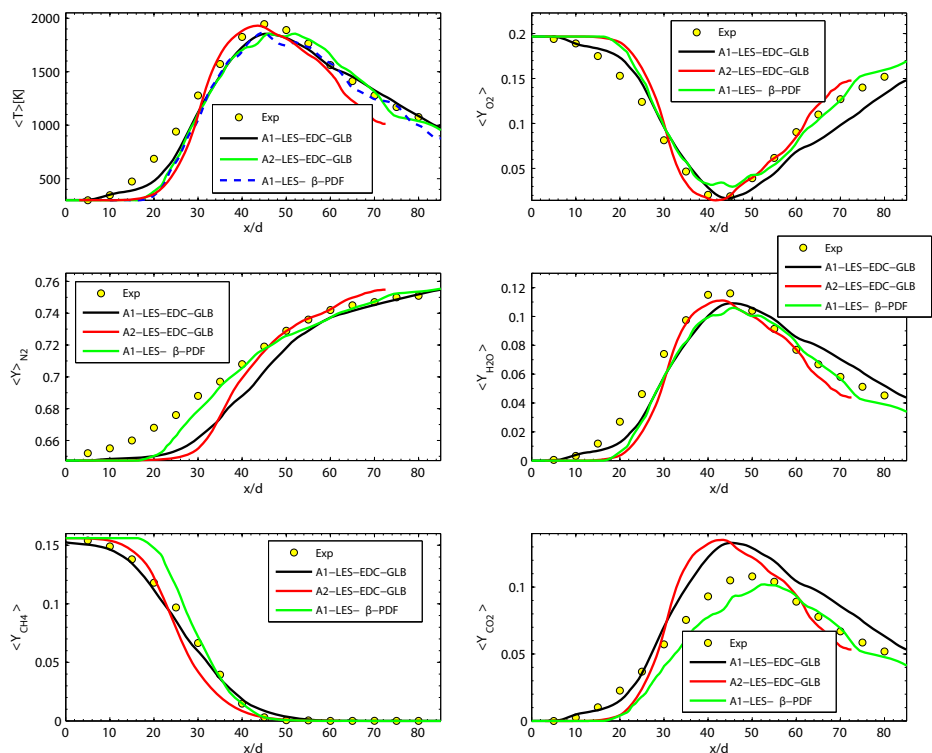


Fig. 12 Mean temperature and composition along the axis for the Sandia Flame D

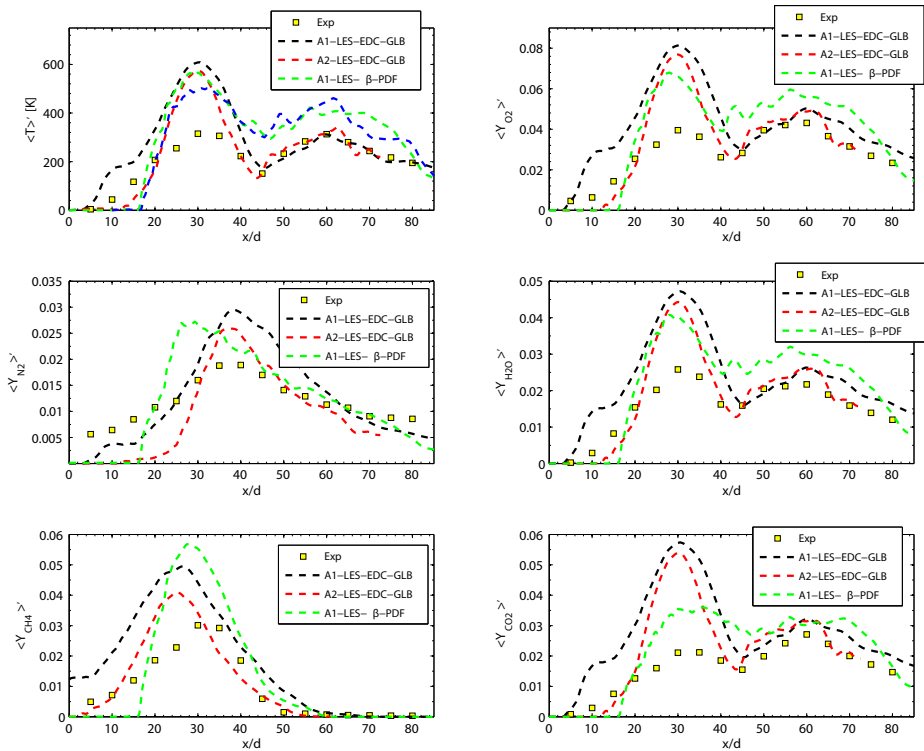


Fig. 13 Fluctuations of mean temperature and composition along the axis for the Sandia Flame D

Agreement between simulations and measured data for the RMS values of N_2 , O_2 , CH_4 and H_2O was reasonable. Behavior of these species have the same trend as for the temperature. The profiles of the RMS values for composition along the axis replicated the behavior of the temperature RMS. The mean mass fraction of CO_2 was slightly over-predicted by both runs.

Figure 14 shows scatter plots of the temperature as a function of mixture fraction by the experiment and the assumed β -PDF approach at three axial distances. The experimental conditional mean of the temperature is shown in Fig. 14 as well. Overall, the agreement between calculations and the experiment was good. One can observe that the maximum

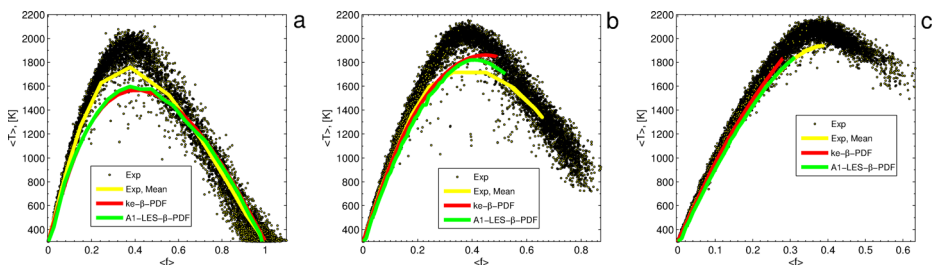


Fig. 14 Scatter plots of temperature versus mixture fraction at three axial locations $x/d = 7.5$ **a**, $x/d = 30$ **b** and $x/d = 45$ **c** for the Sandia Flame D

temperature at $x/d = 7.5$ was under-predicted by approximately 200 K. The match between the predicted and conditional mean temperatures was good up to $\langle f \rangle = 0.5$ and $\langle f \rangle = 0.3$ at $x/d = 30$ and $x/d = 45$, respectively. It is interesting to note that the deviations between the LES-based and the URANS-based results for the β -PDF approach were minimum.

Comparing the single-step RAS results (Fig. 7) with the LES results (Fig. 12), considerable differences are seen. Since the chemistry and turbulence-chemistry interaction models are the same, the differences must mainly result from the flow models. It is well known that round-jet results for RAS, in particular for two-equation models but also for multi-equation models, depend on the choice of constants. Suitable spreading and mixing near the nozzle can be obtained on the cost of poorer results far downstream, or vice versa. The present results indicate that the challenges relate more to flow (turbulence) modeling than to the chemistry and combustion models.

6 Concluding Remarks

The Eddy Dissipation Concept, which has been successfully used in RANS/URANS calculations of turbulent flames has been formulated as a combustion model for the large-eddy simulations and implemented in the OpenFOAM toolbox. The model has been applied both for RAS and LES of the turbulent methane/air combustion for the Sandia flame D. The assumed β -PDF approach was used as well to check the influence of modeling of the turbulence-chemistry interaction. The EDC-based and the β -PDF-based results were compared to the experimental data. It is important, that the present results were obtained without any adjustment or calibration of the model constants and agreement was quite reasonable for all quantities for both RAS and LES predictions. The remaining differences have been discussed. The present RAS/LES results indicate that the disagreement in the numerical results and experiments can be both due to the prediction of turbulence and the use of the turbulence-chemistry interaction sub-models. It is believed that one of the main reasons for the observed discrepancies between the RAS predictions and experimental data was the round-jet anomaly of the standard $k-\epsilon$ turbulence model. The lack of the grid resolution and the insufficient inlet boundary conditions can be considered as the main limitations for the present LES.

Acknowledgments This work was conducted as a part of the CenBio Center for environmentally-friendly energy. The authors would like to thank the Norwegian Meta center for Computational Science (NOTUR) for providing the uninterrupted HPC computational resources and the useful technical support. The authors also gratefully acknowledge the useful correspondence with the reviewers including their suggestions for improvements of this paper.

References

1. ANSYS FLUENT R12. Theory guide. Tech. rep., Ansys Inc (2009)
2. Barlow, R.S., Frank, J.H.: Effects of turbulence on species mass fractions in methane/air jet flames. *Proc. Combust. Inst.* **27**, 1087–1095 (1998)
3. Barlow, R.S., Fiechtner, G.J., Carter, C.D., Chen, J.-Y.: Experiments on the scalar structure of turbulent CO/H₂/N₂ jet flames. *Combust. Flame* **120**, 549–569 (2000)
4. Bowman, C.T., Hanson, R.K., Davidson, D.F., Gardiner, W.C., Lissianski, V., Smith, G.P., Golden, D.M., Frenklach, M., Goldenberg, M.: GRI-Mech (2008). <http://www.me.berkeley.edu/gri-mech/>. Accessed Feb 2013

5. Chase, M.: NIST-JANAF thermochemical tables, 4th edn. In: Journal of Physical and Chemical Reference Data, Monographs and Supplements, vol 9 (1998)
6. Cheng, P.: Dynamics of a radiating gas with application to flow over a wavy wall. *AIAA J.* **4**(2), 238–245 (1966)
7. Dally, B.B., Masri, A.R., Barlow, R.S., Fiechtner, G.J.: Instantaneous and mean compositional structure of bluff-body stabilised nonpremixed flames. *Combust. Flame* **114**, 119–148 (1998)
8. Dunn, M.J., Masri, A.R., Bilger, R.W.: A new piloted premixed jet burner to study strong finite-rate chemistry effects. *Combust. Flame* **151**(1–2), 46–60 (2007)
9. Dunn, M.J., Masri, A.R., Bilger, R.W., Barlow, R.S., Wang, G.H.: The compositional structure of highly turbulent piloted premixed flames issuing into a hot coflow. *Proc. Combust. Inst.* **32**(2), 1779–1786 (2009)
10. Ertesvåg, I.S., Magnussen, B.F.: The eddy dissipation turbulence energy cascade model. *Combust. Sci. Technol.* **159**, 213–235 (2000)
11. Feymark, A., Alin, N., Bensow, R., Fureby, C.: Numerical simulation of an oscillating cylinder using large eddy simulation and implicit large eddy simulation. *J. Fluids Eng.* **134**, 031205 (2012)
12. Frank, J.H., Barlow, R.S., Lundquist, C.: Radiation and nitric oxide formation in turbulent non-premixed jet flames. *Proc. Comb. Inst.* **28**, 447–454 (2000)
13. Garnier, E., Adams, N., Sagaut, P.: *Large Eddy Simulation for Compressible Flows*. Springer, New York (2009)
14. Germano, M., Piomelli, U., Moin, P., Cabot, W.H.: Dynamic subgrid-scale eddy viscosity model. In: Summer Workshop, Center for Turbulence Research, Stanford (1996)
15. Geurts, B.: *Elements of Direct and Large-Eddy Simulation*. R.T. Edwards, Philadelphia (2004)
16. Gran, I.R., Magnussen, B.F.: A numerical study of a bluff-body stabilized diffusion flame. Part 2. Influence of combustion modeling and finite-rate chemistry. *Combust. Sci. Technol.* **119**, 191–217 (1996)
17. Hairer, E., Wanner, G.: *Solving ordinary differential equations II: Stiff and differential-algebraic problems*, Springer Series in Computational Mathematics, 2nd rev. edn. Springer-Verlag (1996)
18. Harten, A.: High resolution schemes for hyperbolic conservation laws. *J. Comput. Phys.* **49**, 357–393 (1983)
19. Hestens, M., Steifel, E.: Methods of conjugate gradients for solving systems of algebraic equations. *J. Res. Nat. Bur. Stand.* **29**, 409–436 (1952)
20. Hewson, J.C., Kerstein, A.R.: Stochastic simulation of transport and chemical kinetics in turbulent CO/H₂/N₂ flames. *Combust. Theory Model.* **5**, 669–897 (2001)
21. Hossain, M., Jones, J.C., Malalasekera, W.: Modelling of a bluff-Body nonpremixed flame using a coupled radiation/flamelet combustion model. *Flow Turbul. Combust.* **67**, 217–234 (2001)
22. Hottel, H.C., Sarofim, A.F.: *Radiative Transfer*. McGraw-Hill, New York (1967)
23. Hutchinson, B., Raithby, G.: A multigrid method based on the additive correction strategy. *J. Numer. Heat. Transf.* **9**, 511–37 (1986)
24. Issa, R.: Solution of the implicitly discretized fluid flow equations by operator splitting. *J. Comput. Phys.* **62**, 40–65 (1986)
25. Jasak, H., Weller, H.G., Gosman, A.D.: High resolution, N.V.D.: differencing scheme for arbitrarily unstructured meshes. *Int. J. Numer. Meth. Fluids* **31**, 431–449 (1999)
26. Jeong, J., Hussain, F.: On the identification of a vortex. *J. Fluid Mech.* **285**, 69–94 (1995)
27. Jones, W.P., Whitelaw, J.H.: Calculation methods for reacting turbulent flows: A review. *Combust. Flame* **48**, 1–26 (1982)
28. Jones, W.P., Prasad, V.N.: Large eddy simulation of the Sandia Flame Series (D-F) using the Eulerian stochastic field method. *Combust. Flame* **157**, 1621–1636 (2010)
29. Launder, B.E., Spalding, D.B.: The numerical computation of turbulent flows. *Comput. Method Appl. M* **3**(2), 269–289 (1974)
30. Lilleberg, B.: On mathematical modeling and numerical simulation of chemical kinetics in turbulent lean premixed combustion, PhD thesis, Norwegian University of Science and Technology, 2011:206, Trondheim (2011)
31. Lilleberg, B., Christ, D., Ertesvåg, I.S., Rian, K.E., Kneer, R.: Numerical simulation with an extinction database for use with the Eddy dissipation concept for turbulent combustion. *Flow Turbul. Combust.* **91**, 319–346 (2013)
32. Lysenko, D.A., Ertesvåg, I.S., Rian, K.E.: Modeling of turbulent separated flows using OpenFOAM. *Comput. Fluids* **80**, 408–422 (2013)
33. Lysenko, D.A., Ertesvåg, I.S., Rian, K.E.: Large-eddy simulation of the flow over a circular cylinder at Reynolds number 3900 using the OpenFOAM toolbox. *Flow Turbul. Combust.* **89**, 491–518 (2012)

34. Lysenko, D.A., Ertesvåg, I.S., Rian, K.E.: Large-eddy simulation of the flow over a circular cylinder at Reynolds number, 2×10^4 . *Flow Turbul. Combust.* **92**, 673–698 (2014)
35. Lysenko, D.A., Ertesvåg, I.S., Rian, K.E., Lilleberg, B., Christ D.: Numerical simulation of turbulent flames using the Eddy dissipation concept with detailed chemistry. In: Skallerud, B., Andersson, H.I. (eds.) *Computational Mechanics*, pp. 159–178. Trondheim (2013)
36. Lysenko, D.A., Ertesvåg, I.S., Rian, K.E.: Numerical simulation of non-premixed turbulent combustion using the Eddy dissipation concept and comparing with the steady laminar flamelet model. *Flow Turbul. Combust.* doi:10.1007/s10494-014-9551-7 (2014)
37. Magnussen, B.F., Hjertager, B.H.: On mathematical modeling of turbulent combustion with special emphasis on soot formation and combustion. *Proc. Combust. Inst.* **16**, 719–729 (1976)
38. Magnussen, B.F.: Modeling of NO_x and soot formation by the Eddy dissipation concept. *Int. flame research foundation, 1st topic oriented technical meeting*, 17–19 Oct. 1989. Amsterdam, Holland
39. Magnussen, B.F.: The Eddy dissipation concept a bridge between science and technology. In: ECCO-MAS Thermal Conference on Computational Combustion. Lisbon (2005)
40. Marshak, R.E.: Note on the spherical harmonics method as applied to the Milne problem for a sphere. *Phys. Rev.* **71**, 443–446 (1947)
41. McGuirk, J.J., Rodi, W.: The calculation of three-dimensional turbulent free jets. In: Durst, F., Launder, B.E., Schmidt, F.W., Whitelaw, J.H. (eds.) *In Turbulent Shear Flows I: Selected Papers from the First International Symposium on Turbulent Shear Flows*, pp. 71–83. Springer-Verlag, Germany (1979)
42. Meijerink, J.A., van der Vorst, H.A.: An iterative solution method for linear systems of which the coefficient matrix is a symmetric M-matrix. *Math. Comput.* **31**, 148–162 (1977)
43. Panjwani, B.: Large Eddy simulation of turbulent combustion with chemical kinetics. PhD thesis, Norwegian University of Science and Technology, 2011:73, Trondheim (2011)
44. Pitsch, H., Steiner, H.: Large-Eddy simulation of a turbulent piloted methane/air diffusion flame (Sandia Flame D). *Phys. Fluids* **12**(10), 2541–2554 (2000)
45. Pitsch, H.: Unsteady flamelet modeling of differential diffusion in turbulent jet diffusion flames original research article. *Combust. Flame* **123**(3), 358–374 (2000)
46. Pope, S.B.: An explanation of the turbulent round-jet/plane-jet anomaly. *AIAA J.* **16**, 279–281 (1978)
47. Raman, V., Pitsch, H., Fox, R.O.: Hybrid large-eddy simulation/Lagrangian filtered-density-function approach for simulating turbulent combustion. *Combust. Flame* **143**, 56–78 (2005)
48. Rhie, C., Chow, W.: Numerical study of the turbulent flow past an airfoil with trailing edge separation. *AIAA J.* **21**, 1525–32 (1983)
49. Sagaut, P.: *Large Eddy simulation for incompressible flows*, 3rd edn. Springer Berlin (2006)
50. Schneider, C., Dreizler, A., Janicka, J., Hassel, E.P.: Flow field measurements of stable and locally extinguishing hydrocarbon-fueled jet flames. *Combust. Flame* **135**, 185–190 (2003)
51. Smith, T.F., Shen, Z.F., Friedman, J.N.: Evaluation of coefficients for the weighted sum of gray gases model. *J. Heat Trans-T. ASME* **104**(4), 602–608 (1982)
52. Vandoormaal, J.P., Raithby, G.D.: Enhancements of the SIMPLE method for predicting incompressible fluid flows. *Numer. Heat Transf.* **7**, 147–163 (1984)
53. Warnatz, J., Maas, U., Dibble, R.W.: *Combustion*, 4th edn. Springer, Berlin Heidelberg New York (2006)
54. Waterson, N.P., Deconinck, H.: Design principles for bounded higher-order convection schemes – a unified approach. *J. Comput. Phys.* **224**, 182–207 (2007)
55. Weller, H.G., Tabor, G., Jasak, H., Fureby, C., tensorial approach to computational continuum mechanics using object-oriented techniques: *Comput. Phys.* **12**(6), 620–631 (1998)
56. Yoshizawa, A.: Statistical theory for compressible shear flows, with the application to subgrid modelling. *Phys. Fluids* **29**(2152), 1416–1429 (1986)
57. Zahirović, S., Scharler, R., Kilpinen, P., Obernberger, I.: Validation of flow simulation and gas combustion sub-models for the CFD-based prediction of NO_x formation in biomass grate furnaces. *Combust. Theory Model.* **15**, 61–87 (2011)